CHEMISTRY
A EUROPEAN JOURNAL

DOI: 10.1002/chem.201000525

A "Neck-Formation" Strategy for an Antiquenching Magnetic/Upconversion Fluorescent Bimodal Cancer Probe

Feng Chen,[a] Shengjian Zhang,[b] Wenbo Bu,*[a] Xiaohang Liu,[b] Yu Chen,[a] Qianjun He,[a] Min Zhu,[a] Lingxia Zhang,[a] Liangping Zhou,[b] Weijun Peng,[b] and Jianlin Shi*[a]

Improving the detection efficiency of early diagnosis by using multimodal nanoprobes is one of the key strategies to win the war against cancer.[1] Most popular nanostructured multimodal imaging probes are combinations of magnetic resonance imaging (MRI) contrast agents, either gadolinium chelates (T_1-imaging) or superparamagnetic iron oxide nanoparticles (SPION, T_2-imaging), and optical imaging probes, such as organic fluorophores, quantum dots (QDs), and lanthanide compounds.[2] Strategies of combining these two modalities can be categorized as chemical linkage route,[3] precipitation method,[4] co-encapsulation technique,[5] electrostatic assembly,[6] epitaxial heterogeneous growth method,[7] and other techniques.[8] Fluorescence quenching, however, is a common problem encountered in the aforementioned strategies.

Safety and excellent optical properties are the two of the primary concerns in the design of satisfactory magnetofluorescent bimodal cancer probes. The use of traditional organic dyes as bioimaging probes remains problematic due to intrinsic drawbacks of high photobleaching rates, short penetration depth, significant autofluorescence, and harmful tissue photodamage.[9] Although some of these problems have been eliminated by using QDs, which have unique optical properties, such as high brightness and photostabilities, large stokes shift, and size-dependent tunable emission, their applications as bioimaging agents remain a great challenge because of the potential cytotoxic risks arising from cadmium (Cd)-containing cores.[10] Upconverting nanoparticles (UCNPs), which emit light at shorter wavelengths after excitation in the near infrared (NIR) region, offer distinct advantages for bioimaging applications due to their better biocompatibility, absolute photostability, negligible background auto-fluorescence, good light penetration depth in tissues and minimum photodamage to the biological specimen.[11] UCNPs have become ideal candidates for optical imaging and very recently great progress has been made by the groups of Hyeon[12a] and Prasad[12b] in combining T_1-weighted MR imaging with upconversion fluorescence through thermal decomposition synthesis of erbium (Er^{3+}), ytterbium (Yb^{3+}) and gadolinium (Gd^{3+}) tri-doped $NaYF_4$ nanocrystals, designated as UCNP(Er, Yb, Gd).[12] However, the potential toxicity of such Gd^{3+}-containing novel bimodal imaging agent still provokes safety concerns. Therefore, the integration of a more biocompatible T_2-weighted MRI contrast agent with UCNPs by forming a better-designed, Cd^{2+}- and Gd^{3+}-free, antiquenching, multifunctional, nano cancer probe still remains in a great need for the early cancer diagnosis.

To make a reliable bimodal diagnosis, a solid linkage between magnetic and fluorescent agents is necessary. However, direct combination between SPION and UCNP could lead to serious undesirable problems, such as fluorescent quenching of UCNP by a neighboring SPION and the loss of superparamagnetic properties of SPIONs by the oriented attachment among themselves.[13] Therefore, the most ideal combination without aforementioned problems might be to first protect the SPION and UNCP, and then from a solid bridge between them.

A "neck-formation" process, which is induced by condensation of residual ≡Si-OH groups on the surface of silica-containing particles and formation of the siloxane bridges ≡Si-O-Si≡ between particles, as shown in Figure S1 in the

[a] F. Chen, Prof. W. Bu, Y. Chen, Q. He, M. Zhu, Prof. L. Zhang, Prof. J. Shi
State Key Laboratory of High performance Ceramics and Superfine Microstructures, Shanghai Institute of Ceramics Chinese Academy of Sciences, Shanghai, 200050 (P.R. China)
Fax: (+86)-21-52413122
E-mail: jlshi@sunm.shcnc.ac.cn
wbbu@mail.sic.ac.cn

[b] S. Zhang, X. Liu, L. Zhou, Prof. W. Peng
Department of radiology, Shanghai Cancer hospital
Fudan University, Shanghai, 200032, (P.R. China)

Supporting information for this article is available on the WWW under http://dx.doi.org/10.1002/chem.201000525.

Supporting Information, is a common phenomenon in the silica chemistry.[5f–h,14] Since the first synthesis of silica microspheres by the classic Stöber method in 1968,[14f] such phenomena have been considered to be greatly harmful to the monodispersity of both SiO_2 and cores@silica shell hybrid nanoparticles, due to its uncontrolled aggregation and greatly broadened size distribution. Especially, aggregated particles with sizes larger than 300 nm are no longer considered to be safe for use in veins due to possible thrombosis.[15] Could such a neck-formation process, with careful control over the whole synthetic process, be used to fabricate a magnetofluorescent, bimodal cancer probe with different imaging modalities being well-separated from but firmly connected with each other? Here in this communication, as shown in Scheme 1, this idea is demonstrated by applying a neck-formation process to fabricate silica-shielded, magnetic upconversion, fluorescent oligomers (SMUFOs) with controlled particle size and size distribution. The proposed synthetic strategy differs from our previously reported methods for core@shell hybrid functional nanostructures,[16] and the extensively adopted co-encapsulation techniques,[5] in which different functional nanoparticles are entrapped randomly in the matrix without the necessary protection from direct particle contact. The whole process for the controlled neck-formation strategy is illustrated in Scheme 1. After the addition of carefully designated amounts of cyclohexane, Igepal CO-520, SPION, UCNP, and ammonia, the whole system was well-sealed, and kept at 20 °C (open system and higher temperature would lead to severe and uncontrollable aggregations).[16e] To improve the reproducibility, suppress the homogeneous nucleation of silica, and avoid the over-high local concentration of precursors, clinically approved syringe pump (WZS-50F6) was used to deliver tetraethylorthosilicate (TEOS) slowly (at a rate of 1.0 mL h^{-1}) and accurately (step 1). Upon the injection of TEOS, base-catalyzed hydrolysis and condensation of the TEOS precursor takes place, followed by the heterogeneous nucleation and growth of silica shells on the SPION and UCNP seeds, which results in single-loaded structures of SPION@SiO_2 and UCNP@SiO_2 with residual ≡Si-OH groups on their surfaces (step 2). Detailed procedures on the incorporation of single seeds into a silica matrix can be referred in our newly-published work.[16e] Then the system went through a controlled neck-formation process, in which single-loaded SPION@SiO_2 and UCNP@SiO_2 nanoparticles combine through the cross-linked ≡Si-O-Si≡ network, forming a solid linkage of $\{SPION@SiO_2\}_m$-Si-O-Si-$\{UCNP@SiO_2\}_n$ ($m>0$, $n>0$) with limited values of m and n, with controlled size distribution of the composite structure (step 3).

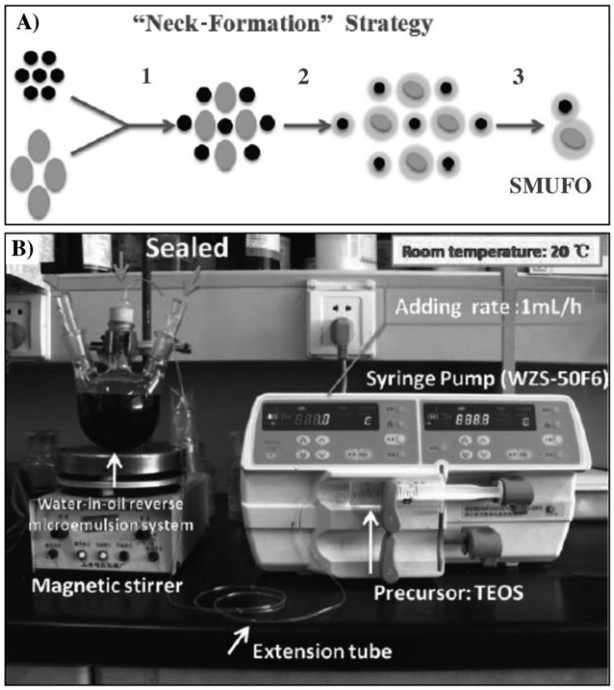

Scheme 1. A) Schematic illustration showing the formation of SMUFO in the W/O reverse microemulsion system by means of a neck-formation strategy. After the addition of carefully designated amounts of cyclohexane, Igepal CO-520, SPION, UCNP, and ammonia into the W/O system, the whole system was well-sealed, and kept at 20 °C (step 1). A clinically used syringe pump (WZS-50F6) was used to deliver TEOS slowly (at a rate of 1.0 mL h^{-1}) and accurately (see Scheme 1 B). Upon injection of TEOS, base-catalyzed hydrolysis and condensation of the TEOS precursor took place, and then heterogeneous nucleation and growth of silica shells on the SPION and UCNP seeds occurred, resulting in single-loaded structures of SPION@SiO_2 and UCNP@SiO_2 with residual ≡Si–OH groups on their surface (step 2). Then the system went through a neck-formation process, in which SPION@SiO_2 and UCNP@SiO_2 nanoparticles are combined by means of the cross-linked ≡Si-O-Si≡ network, forming complex $\{SPION@SiO_2\}_m$-Si-O-Si-$\{UCNP@SiO_2\}_n$ (m, $n>0$) structures with limited values of m and n (step 3). B) An experimental setup for the synthesis of SMUFO; (see Supporting Information for color version of Scheme 1.)

Monodisperse spherical SPION and irregularly-shaped UCNP(Er,Yb) were prepared before introducing to the reverse micro-emulsion medium for silica coating (Supporting Information: Figures S2 and S3). Figure 1A1–A3 present the TEM images of ≈13 nm-sized SPION, ≈20 nm-sized UCNP (Er,Yb), and their mixture, respectively. TEM images in Figure 1A4–A6 reveal the core/shell peanut-like or dumbbell-like structures of SMUFOs (shell thickness: ≈5 nm), in which single-loaded SPION@SiO_2 and UCNP@SiO_2 have been integrated together through silica solid "necks", but not detachable particle "overlaps" (Figure S4 in the Supporting Information shows the differences between neighboring particle "overlaps" and silica "necks"). The thickness of silica shell could be easily adjusted from 5 to 10 nm by increasing the volume of TEOS used (Figure 1A7–A9). The high-resolution TEM (HRTEM) image (Figure 1 B) clearly shows that both core components are single crystalline and are well "separated" but firmly "linked" by solid silica "necks" (marked by arrows). Figure 1 B also shows the parallel lattice planes for SPION and UCNP(Er,Yb), with their lattice spacings of 4.850 and 3.150 Å, respectively, which correspond to the (111) lattice planes of both cores. Selected area electron diffraction patterns from these structures (Figure 1 B, insert) show ring patterns from the cubic spinel and cubic structures of Fe_3O_4 and α-$NaYF_4$, respectively (more details could be found in Figure S5 in the Supporting Infor-

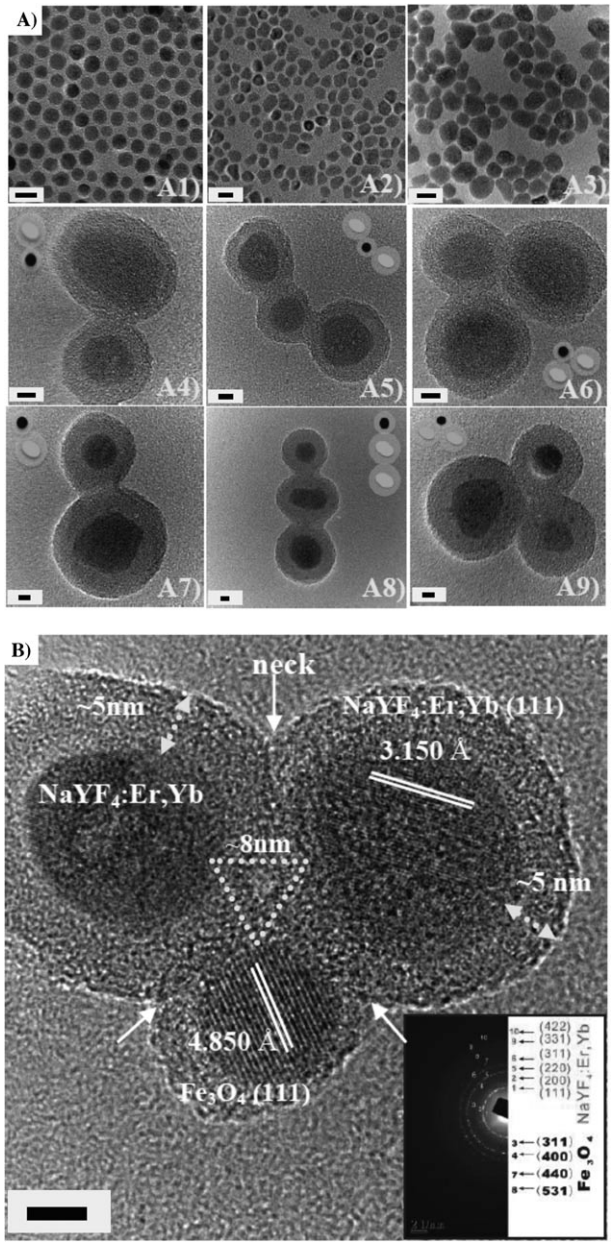

Figure 1. TEM images of A1) SPION; A2) UCNP(Er,Yb); A3) SPION and UCNP(Er,Yb) mixture (scale bar: 20 nm). TEM images of as-synthesized SMUFO with different shell thicknesses of A4)–A6) ≈5 nm, and A7)–A9) ≈10 nm (scale bar: 5 nm). Inserts in A4–A9 are the schematic illustrations of SMUFO. B) HR-TEM image of as obtained SMUFO; necks are marked by arrows (scale bar: 5 nm). Insert: the electron diffraction pattern of SMUFO. (See Supporting Information for a color version of Figure 1.)

mation). XRD patterns confirmed the existence of Fe_3O_4, α-$NaYF_4$:Er,Yb and amorphous SiO_2 (Figure S6 in the Supporting Information). Energy dispersive X-ray analysis also reveals the elemental signals from the SMUFOs (Figure S7 in the Supporting Information). A low-magnification TEM image of SMUFO in Figure S8 A in the Supporting Information shows that most of the SPION@SiO_2 and UCNP@SiO_2 nanoparticles are linked together through the solid silica necks with limited m and n values, while a small fraction of free SPION@SiO_2 and UCNP@SiO_2 structures could still be observed in the image. Correspondingly, the dynamic light scattering (DLS) measurement demonstrated that the average hydrodynamic size of the SMUFOs in deionized water was 114.8 nm (Figure S8 B in the Supporting Information). It is important to note that the size distribution is still relatively sharp after neck formation, implying that the neck-formation process is controllable, and most aggregates formed in the process are composed of limited numbers of single-loaded SPION@SiO_2 and UCNP@SiO_2 nanoparticles. The maximum particle size is smaller than 250 nm, which is vitally important for the in vivo applications of the nanoparticles in blood.[15] Hence, a bimodal probe with two different modalities entrapped in silica matrix has been successfully synthesized.

The field-dependent magnetism of SMUFO (silica shell thickness: ≈5 nm) at 300 K in Figure 2 A (black line) shows no hysteresis and a saturation magnetization of 89.8 emu g^{-1} Fe, close to that of pure SPION (92.5 emu g^{-1} Fe, Figure S3-B in the Supporting Information), demonstrating its super-paramagnetism, which is a necessary characteristic for T_2-weighted MR contrast agents for practical use. Under the excitation in near infrared ($\lambda =$

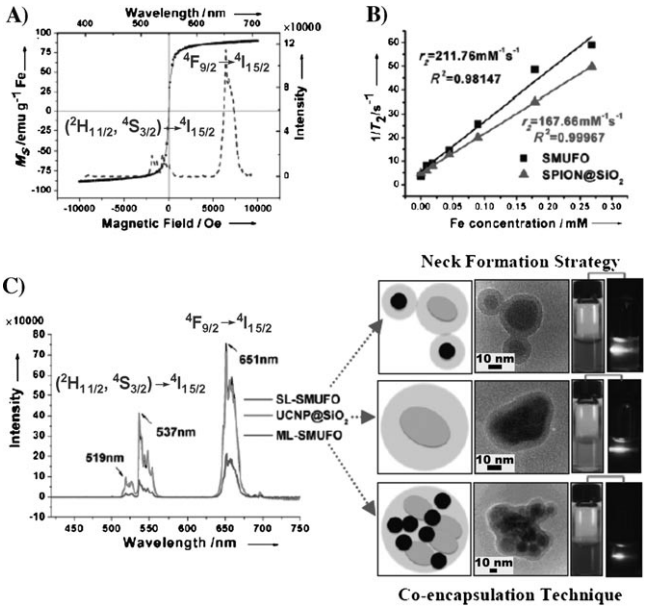

Figure 2. A) Field-dependent magnetization hysteresis loop of SMUFO at 300 K (solid line, $M_s = 89.9$ emu g^{-1} Fe) and upconversion luminescence spectrum of SMUFO with green (510–560 nm) and red (635–690 nm) emission bands (excited with a 980 nm laser, dash line). B) Plots of inverse transverse relaxation times ($1/T_2$) versus Fe concentration: SPION@SiO_2 (▲) and SMUFO (■). The slope indicates the T_2 relaxivity coefficient (r_2). C) Room-temperature upconversion luminescence spectra of SL-SMUFO, UCNP@SiO_2 and ML-SMUFO with the same concentrations of Y (250 μg mL^{-1}) and similar silica shell thickness (≈5 nm; excited with a 980 nm laser, power ≈438 mW). Insert: schematic (left), TEM images (middle) and corresponding photographs of SL-SMUFO, UCNP@SiO_2 and ML-SMUFO under natural light and 980 nm laser (right, power ≈314 mW). (See Supporting Information for color version of Figure 2.)

980 nm), as-synthesized SMUFO shows green emission bands at $\lambda = 510$–560 nm, and red emission bands at 635–690 nm, which could be assigned to the feature transitions from $^2H_{11/2}$, $^4S_{3/2}$, and $^4F_{9/2}$ to $^4I_{15/2}$ of Er^{3+} ions, respectively (Figure 2A, blue line).[17] The T_2-MR contrast effect of SMUFO was examined in comparison with that of single-loaded SPION@SiO_2 with the same iron (Fe) concentrations (Figures S8 and S9 in the Supporting Information). In the T_2-weighted MRI at 3.0 T, SPION@SiO_2 showed a high enough MR contrast with a T_2 relaxivity coefficient (r_2) of 167.66 $mM^{-1}s^{-1}$, while SMUFO provided an even higher MR contrast with 1.3-fold increased r_2 value of 211.76 $mM^{-1}s^{-1}$ (Figure 2B). Such an enhancement in r_2 could be attributed to synergistic magnetism[3c,18] of multiple SPION in our SMUFO hybrid structure. In addition, as-synthesized SMUFO shows high stabilities in respects of both the fluorescent and magnetic properties. The fluorescent intensity of the sample kept for one month showed only a limited decrease, about 15.4 and 7.7% for green (537 nm) and red (651 nm) emissions, respectively (Figure S10 in the Supporting Information), and the T_2 relaxivity coefficient (r_2) of SMUFO after dispersed in deionized water for four months was found to be 217.23 $mM^{-1}s^{-1}$, close to the original value of 211.76 $mM^{-1}s^{-1}$ of the fresh sample (Figure S11 in the Supporting Information).

Previous reports have shown that the combination of QDs with SPION through either direct chemical bond linkage[3g] or co-encapsulation technique[5m] (without any preliminary protections) could lead to apparent decrease of quantum yield, indicating that the particle interaction might have great influence on the optical property of the as-synthesized bimodal probes. To demonstrate this particle-interaction effect and the antiquenching property of as-obtained SMUFO, upconversion luminescent spectra of SMUFO (also labeled as single-loaded SMUFO (SL-SMUFO)), UCNP@SiO_2 and multi-loaded SMUFO (ML-SMUFO) with the same yttrium concentrations (250 $\mu g\,mL^{-1}$) and similar shell thickness ($\approx$5 nm) were collected under the same 980 nm excitation (power $\approx$438 mW). It was clearly shown in Figure 2C that three Er^{3+} emission band intensities of SL-SMUFO were very close to those of UCNP@SiO_2, but remarkably higher than those of ML-SMUFO. The intensity ratios of three samples at 519 nm ($^2H_{11/2}\rightarrow{}^4I_{15/2}$), 537 nm ($^4S_{3/2}\rightarrow{}^4I_{15/2}$), 651 nm ($^4F_{9/2}\rightarrow{}^4I_{15/2}$) were calculated to be: ${}^{SL\text{–}SMUFO}I_{519nm}:{}^{UCNP@SiO_2}I_{519nm}:{}^{ML\text{–}SMUFO}I_{519nm} = 0.95:1.00:0.18$; ${}^{SL\text{–}SMUFO}I_{537nm}:{}^{UCNP@SiO_2}I_{537nm}:{}^{ML\text{–}SMUFO}I_{537nm} = 0.93:1.00:0.20$; ${}^{SL\text{–}SMUFO}I_{651nm}:{}^{UCNP@SiO_2}I_{651nm}:{}^{ML\text{–}SMUFO}I_{651nm} = 1.05:1.00:0.29$.

These experimental results demonstrated that: 1) UCNP shows excellent resistance to photoquenching after the introduce of SPION by means of the neck-formation strategy; 2) particle-interaction is one of the major reasons for photoquenching of UCNP, and 3) the neck-formation strategy is superior to co-encapsulation technique for achieving antiquenching imaging probes.

The bimodal imaging functionality of SMUFO in aqueous solution was tested using a 3.0 T clinical MRI instrument and 980 nm laser. Figure 3A displays the Fe concentration-dependent T_2-MR contrast effect, in which higher Fe concentrations, from 0 to 20 $\mu g\,Fe\,mL^{-1}$, gave darker images and smaller spin–spin relaxation times (T_2), from 275.7 to 15.8 ms, respectively. Excessively high Fe concentrations (over 40 $\mu g\,Fe\,mL^{-1}$) led to undetectable T_2 values (marked by crosses in Figure 3A). SMUFO with different concentrations of Y, from 0 to 261.2 $\mu g\,Y\,mL^{-1}$, shows expected increased fluorescent intensity under the same 980 nm laser excitation, as shown in Figure 3A. The magnetic separability and gram-scale (1.3799 g) synthesis of SMUFO were also demonstrated in Figure 3B and C.

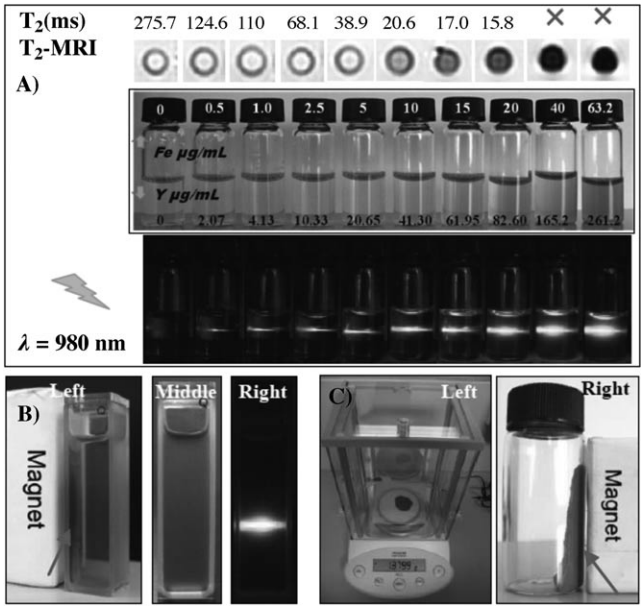

Figure 3. A) Bimodal imaging test of SMUFO in aqueous solution. The concentrations of Fe and Y in SMUFO were in the range 0–63.2 $\mu g\,Fe\,mL^{-1}$ and 0–261.2 $\mu g\,Y\,mL^{-1}$, respectively. From the top down: T_2 values, corresponding T_2-MR images, photographs under natural light and under 980 nm laser (power $\approx$314 mW) of samples with different Fe and Y concentrations. Excessively high Fe concentrations (over 40 $\mu g\,Fe\,mL^{-1}$) led to undetectable T_2 values (marked by crosses). B) Photographs of magnetic separation of SMUFO in ethanol (left, marked by arrow); SMUFO under natural light (middle) and 980 nm laser (right; power $\approx$314 mW). C) Photographs of as-synthesized 1.3799 g SMUFO dry powder (left) and that with a magnet (right). (See Supporting Information for color version of Figure 3.)

To evaluate the possible cytotoxicity of SMUFO, cell viability was examined by standard 3-[4,5-dimethylthialzol-2-yl]-2,5-diphenyltetrazolium bromide (MTT) assay in human breast cancer cells, which revealed that the cytotoxicity was dose- and time-dependent. Cell viability was not hindered by the presence of SMUFO up to a concentration of 25 $\mu g\,mL^{-1}$ for 6 h incubation, while it shows slight and limited toxicity in the case of higher concentration of SMUFO and longer incubation time, as shown in Figure S12 in the Supporting Information. The as-synthesized SMUFO has multiple functionalities applicable for multimodal imaging of cancer cells. In vitro bimodal imaging of SMUFO was demonstrated in the MCF-7 breast cancer cell line. Under the T_2-weighted image mode, cells exposed to SMUFO of

concentrations higher than 200 μg mL^{-1} for 2 h could be easily detected (Figure 4 A, marked by circles). Confocal luminescence imaging of MCF-7 cells was performed with a modified Olympus FV1000 laser-scanning confocal microscope (LSCM), equipped with a continuous-wave (CW) NIR laser operated at $\lambda = 980$ nm (power ≈ 400 mW). Figure 4 B reveals the uptake of SMUFO was concentration-dependent (incubation time: 2 h), and could be clearly observed when the SMUFO concentration was higher than 200 μg mL^{-1}, in agreement with the T_2-weighted MRI results.

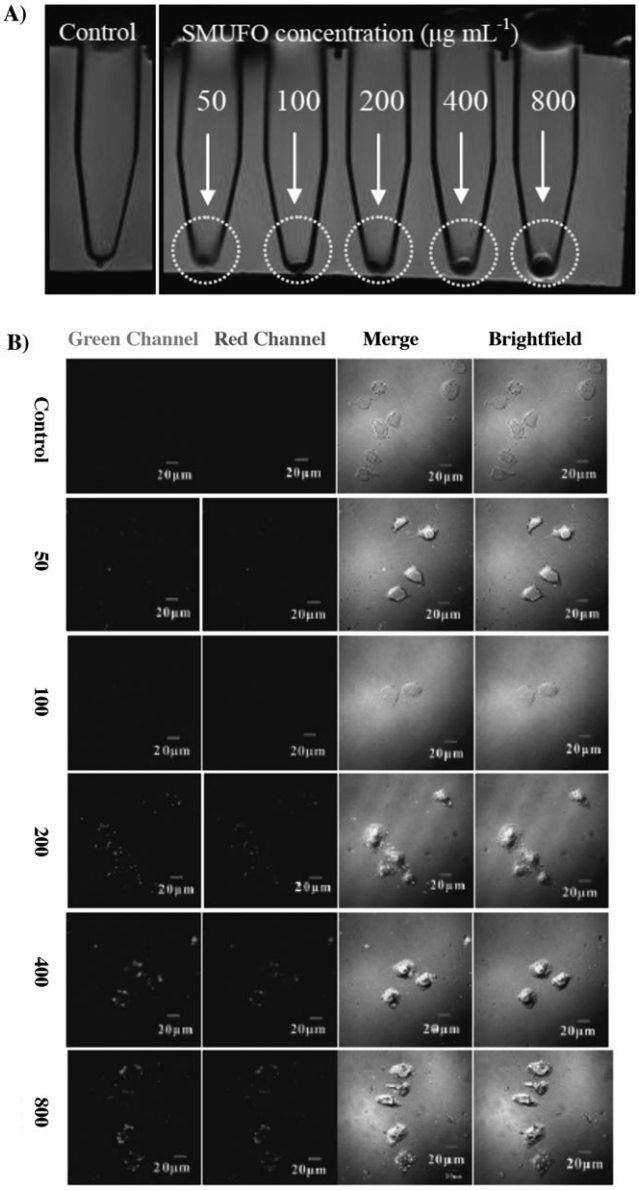

Figure 4. In vitro bimodal imaging of breast cancer cells (MCF-7) using SMUFO. A) Sensitivity of in vitro MRI of SMUFO. MCF-7 with cell density of 10^6 per well were treated with SMUFO of different concentrations (from 50–800 μg mL^{-1}). Unlabeled cells of identical number were scanned as a control group (left). The cells could be detected as black areas at tube bottoms (marked by circles), which resembles cell distribution visualized in these test tubes. B) Confocal images of MCF-7 cells incubated with SMUFO of concentration range 50–800 μg mL^{-1} were obtained by using a modified Olympus FV1000 laser-scanning confocal microscope (LSCM), equipped with a continuous-wave (CW) NIR laser operating at $\lambda = 980$ nm (power ≈ 400 mW). Green channel images were collected at 500–560 nm, while red channel images were collected at 600–700 nm; scale bars = 20 μm. (See Supporting Information for color version of Figure 4.)

To demonstrate the feasibility of SMUFO as a bimodal imaging probe in vivo, we simply subcutaneously injected the probe right into the tumor site, and imaged the tumor using MRI instrument and NIR laser. Following the local injection of SMUFO at a dose of 240 μg Fe kg^{-1} (equal to 992 μg Y kg^{-1}, 25.4 μg Er kg^{-1}), the SD mouse bearing a Walker 256 tumor was then imaged on the 3.0 T MRI instrument. Preinjection T_2-map was shown in Figure 5 A (top)

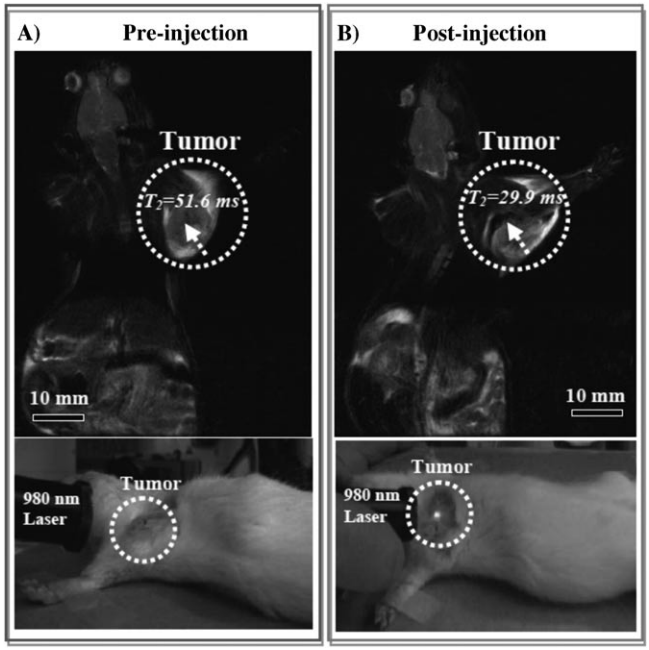

Figure 5. In vivo MR and upconversion fluorescence bimodal imaging of Walker 256 tumor using SMUFO. In vivo whole body pre-injection (A top, tumor was marked with circle, $T_2 = 51.6$ ms), and post-injection (B top, tumor was marked with circle, $T_2 = 29.9$ ms) MRI of mouse bearing a Walker 256 tumor. Pre-injection image (A bottom) and post-injection image (B bottom) of the upconversion fluorescence imaging of tumor in vivo using NIR laser ($\lambda = 980$ nm). Images were taken with a digital camera (CANON PowerShot G7). (See Supporting Information for color version of Figure 5.)

with a T_2-value in the tumor site (marked with a circle) of 51.6 ms. After the injection of SMUFO, a continuous T_2 value drop of 42.2 %, from 51.6 ms to 29.8 ms, is observed within 5 min (Figure 5 B (top), marked with a circle), demonstrating that SMUFO could be used as a T_2 contrast agent in the live system. Autofluorescence can be problematic in the diagnosis of cancer using the fluorophore of interest. Figure S13 in the Supporting Information shows the imaging of tumor using CdTe QDs under blue light excitation ($\lambda =$ 405 nm), in which signals of CdTe QDs could hardly be distinguished from the severe tissue autofluorescence. This

problem could be solved by introducing a NIR excitation to prevent tissue from being excited.[11e,19] After the NIR ($\lambda =$ 980 nm) excitation, the emission signals of SMUFO in tumor site could be easily seen by naked eyes and recorded with a digital camera (CANON PowerShot G7), as shown in Figure 5B (bottom). To the best of our knowledge, this is the first example of simultaneous in vivo MR and upconversion fluorescent bimodal imaging of a tumor. The design of a smarter antibody-conjugated, tumor-targeted, bimodal imaging probe are in progress.

In comparison with previous reports,[3–8] three features of as-synthesized SMUFO become clear.

1) Biocompatible SPION with nontoxic Cd^{2+}- and Gd^{3+}-free UCNP(Er,Yb) have been combined by means of a novel and controlled neck-formation mechanism for a safer bimodal cancer probe, which shows a relatively sharp size distribution at around 114 nm, high stability, an enhanced T_2-weighted MR contrast effect and excellent antiquenching upconversion fluorescent optical properties.
2) Highly hydrophilic silica shells, which act as a barrier, make the composite systems highly soluble in aqueous solutions, and could also effectively shield both inorganic cores against the attack from biological environment, and more importantly, prevent the UCNP(Er,Yb) from photoquenching by separating the cores from each other.
3) The proposed general neck-formation strategy is economical (all chemical agents are commercially available, nontoxic, and inexpensive, see Figure S14 in the Supporting Information for chemical agents used), scalable (see Scheme 1B for experimental setup), and even tunable (not only the loaded cores but also the thickness and extra functionalities of silica shells can be conveniently tuned and modified—data not shown), showing the great potential of the present nanosystems as a novel, biologically safe and highly efficient, bimodal cancer probe for clinical use and future industrialization.

Combining black SPION with fluorescent nanoparticles to fabricate an efficient bimodal cancer probe without inviting any undesired quenching process is still an open challenge. In our present work, by making use of a traditionally undesired neck-formation process, we have been successful in synthesizing a bimodal cancer probe with satisfactory antiquenching properties. However, since the formation of SMUFO by the condensation of residual surface ≡Si–OH groups is based on a random aggregating process so far, the proposed neck-formation strategy is still not perfect to obtain SMUFO with extremely high uniformity. Fortunately, thanks to the original small particle sizes of well under 100 nm of both SPION@SiO_2 and UCNP@SiO_2 hybrid structures, we have succeeded in monitoring the neck-formation process with a final well-defined particle size distribution (measured by DLS technique) centered at about 114 nm, by the careful control over the whole synthetic process. The maximum particle size in the obtained SMUFO system is well below 300 nm, which has been considered to be a critical particle size for vein injection. In addition, since the non-uniformity of the present SMUFO is well on the scale of tens or one hundred nanometers, it is applicable for SMUFO to be used as a bimodal imaging agent for simultaneous MRI and fluorescence imaging (both usually on resolution levels of tens or hundreds of micrometers), as demonstrated in Figures 3–5.

In summary, we have demonstrated that bimodal cancer imaging agent with both T_2-weighted MR and upconversion fluorescent imaging modalities can be prepared by means of a simple, economical, scalable, and tunable neck-formation strategy. As-synthesized cadmium- and gadolinium-free SMUFO show a well-controlled size distribution, with the maximum particle size being less than 250 nm, with high photo and magnetic stability, enhanced T_2-weighted MR imaging, and with quenchless upconversion fluorescent properties. Its application as a bimodal breast cancer cell imaging probe has been demonstrated both in vitro and in vivo. We believe that as-synthesized, biologically safe and highly efficient, bimodal probes hold great potential for future early cancer diagnosis and the proposed neck-formation strategy could open a new possibility for the targeted design and synthesis of various multifunctional nanosystems.

Experimental Section

For experimental details please see the Supporting Information. Procedures performed by using animals were conducted in agreement with the guidelines of the Institutional Animal Care and Use Committee.

Acknowledgements

We thank Jing Zhou, Yuan Gao and Professor Fuyou Li, from Department of Chemistry, Fudan University, for the confocal luminescence imaging and in vivo imaging tests. We thank Meiling Ruan, Jingwei Feng, Lingling Zhang, Yan Yang, from Shanghai Institute of Ceramics Chinese Academy of Sciences, for TEM and optical analysis, and Yuchi Fan, Jianan Liu, Huaiyong Xing, and Moying Chen for thoughtful discussions. This work has been financially supported by the National Natural Science Foundation of China Research (Grant No. 50972154, 50672115, 50823007), the Shanghai Rising-Star Program (Grant No. 07A14061), the Shanghai Nano-special Project (Grant No. 0852nm03900), and CASKJCX Projects (Grant No. KJCX2.YW.M02 and KJCX2-YW-210).

Keywords: antitumor agents · fluorescence · imaging agents · magnetic resonance imaging · neck formation

[1] a) P. Rivera Gil, W. J. Parak, *ACS Nano* **2008**, *2*, 2200–2205; b) Y. Piao, A. Burns, J. Kim, U. Wiesner, T. Hyeon, *Adv. Funct. Mater.* **2008**, *18*, 3745–3758; c) Y. W. Jun, J. H. Lee, J. Cheon, *Angew. Chem.* **2008**, *120*, 5200–5213; *Angew. Chem. Int. Ed.* **2008**, *47*, 5122–5135.

[2] a) J. Kim, Y. Piao, T. Hyeon, *Chem. Soc. Rev.* **2009**, *38*, 372–390; b) A. Quarta, R. Di Corato, L. Manna, A. Ragusa, T. Pellegrino, *IEEE Trans. Nanobiosci.* **2007**, *6*, 298–308.

[3] a) C. G. Wang, J. Chen, T. Talavage, J. Irudayaraj, *Angew. Chem.* **2009**, *121*, 2797–2801; *Angew. Chem. Int. Ed.* **2009**, *48*, 2759–2763; b) B. Fernández, N. Galvez, R. Cuesta, A. B. Hungria, J. J. Calvino, J. M. Dominguez-Vera, *Adv. Funct. Mater.* **2008**, *18*, 3931–3935; c) J. H. Lee, Y. W. Jun, S. I. Yeon, J. S. Shin, J. Cheon, *Angew. Chem.* **2006**, *118*, 8340–8342; *Angew. Chem. Int. Ed.* **2006**, *45*, 8160–8162; d) J. H. Gao, L. Li, P. L. Ho, G. C. Mak, H. W. Gu, B. Xu, *Adv. Mater.* **2006**, *18*, 3145–3148; e) H. S. Yang, S. Santra, G. A. Walter, P. H. Holloway, *Adv. Mater.* **2006**, *18*, 2890–2894; f) O. Veiseh, C. Sun, J. Gunn, N. Kohler, P. Gabikian, D. Lee, N. Bhattarai, R. Ellenbogen, R. Sze, A. Hallahan, J. Olson, M. Q. Zhang, *Nano Lett.* **2005**, *5*, 1003–1008; g) D. S. Wang, J. B. He, N. Rosenzweig, Z. Rosenzweig, *Nano Lett.* **2004**, *4*, 409–413.

[4] a) Z. Y. Ma, D. Dosev, M. Nichkova, S. J. Gee, B. D. Hammock, I. M. Kennedy, *J. Mater. Chem.* **2009**, *19*, 4695–4700; b) H. C. Lu, G. S. Yi, S. Y. Zhao, D. P. Chen, L. H. Guo, J. Cheng, *J. Mater. Chem.* **2004**, *14*, 1336–1341.

[5] a) P. Yang, Z. Quan, Z. Hou, C. Li, X. Kang, Z. Cheng, J. Lin, *Biomaterials* **2009**, *30*, 4786–4795; b) Z. Y. Liu, G. S. Yi, H. T. Zhang, J. Ding, Y. W. Zhang, J. M. Xue, *Chem. Commun.* **2008**, 694–696; c) M. Liong, J. Lu, M. Kovochich, T. Xia, S. G. Ruehm, A. E. Nel, F. Tamanoi, J. I. Zink, *ACS Nano* **2008**, *2*, 889–896; d) J. Kim, H. S. Kim, N. Lee, T. Kim, H. Kim, T. Yu, I. C. Song, W. K. Moon, T. Hyeon, *Angew. Chem.* **2008**, *120*, 8566–8569; *Angew. Chem. Int. Ed.* **2008**, *47*, 8438–8441; e) N. Insin, J. B. Tracy, H. Lee, J. P. Zimmer, R. M. Westervelt, M. G. Bawendi, *ACS Nano* **2008**, *2*, 197–202; f) C. W. Lu, Y. Hung, J. K. Hsiao, M. Yao, T. H. Chung, Y. S. Lin, S. H. Wu, S. C. Hsu, H. M. Liu, C. Y. Mou, C. S. Yang, D. M. Huang, Y. C. Chen, *Nano Lett.* **2007**, *7*, 149–154; g) W. J. Rieter, J. S. Kim, K. M. L. Taylor, H. Y. An, W. L. Lin, T. Tarrant, W. B. Lin, *Angew. Chem. Int. Ed.* **2007**, *119*, 3754–3756; *Angew. Chem. Int. Ed.* **2007**, *46*, 3680–3682; h) J. L. Bridot, A. C. Faure, S. Laurent, C. Riviere, C. Billotey, B. Hiba, M. Janier, V. Josserand, J. L. Coll, L. Vander Elst, R. Muller, S. Roux, P. Perriat, O. Tillement, *J. Am. Chem. Soc.* **2007**, *129*, 5076–5084; i) H. Lee, M. K. Yu, S. Park, S. Moon, J. J. Min, Y. Y. Jeong, H.-W. Kang, S. Jon, *J. Am. Chem. Soc.* **2007**, *129*, 12739–12745; j) J. Kim, J. E. Lee, J. Lee, J. H. Yu, B. C. Kim, K. An, Y. Hwang, C. H. Shin, J. G. Park, T. Hyeon, *J. Am. Chem. Soc.* **2006**, *128*, 688–689; k) D. K. Yi, S. T. Selvan, S. S. Lee, G. C. Papaefthymiou, D. Kundaliya, J. Y. Ying, *J. Am. Chem. Soc.* **2005**, *127*, 4990–4991; l) S. Santra, R. P. Bagwe, D. Dutta, J. T. Stanley, G. A. Walter, W. Tan, B. M. Moudgil, R. A. Mericle, *Adv. Mater.* **2005**, *17*, 2165–2169; m) S. Santra, H. S. Yang, P. H. Holloway, J. T. Stanley, R. A. Mericle, *J. Am. Chem. Soc.* **2005**, *127*, 1656–1657; n) Z. Li, Y. Zhang, B. Shuter, N. Muhammad Idris, *Langmuir* **2009**, *25*, 12015–12018.

[6] a) B. Sun, Y. Zhang, K. J. Gu, Q. D. Shen, Y. Yang, H. Song, *Langmuir* **2009**, *25*, 5969–5973; b) J. S. Kim, W. J. Rieter, K. M. L. Taylor, H. An, W. L. Lin, W. B. Lin, *J. Am. Chem. Soc.* **2007**, *129*, 8962–8963; c) V. Salgueiriño-Maceira, M. A. Correa-Duarte, M. Spasova, L. M. Liz-Marzan, M. Farle, *Adv. Funct. Mater.* **2006**, *16*, 509–514.

[7] a) S. H. Choi, H. Bin Na, Y. Park Il, K. An, S. G. Kwon, Y. Jang, M. Park, J. Moon, J. S. Son, I. C. Song, W. K. Moon, T. Hyeon, *J. Am. Chem. Soc.* **2008**, *130*, 15573–15580; b) S. T. Selvan, P. K. Patra, C. Y. Ang, J. Y. Ying, *Angew. Chem.* **2007**, *119*, 2500–2504; *Angew. Chem. Int. Ed.* **2007**, *46*, 2448–2452; c) W. L. Shi, H. Zeng, Y. Sahoo, T. Y. Ohulchanskyy, Y. Ding, Z. L. Wang, M. Swihart, P. N. Prasad, *Nano Lett.* **2006**, *6*, 875–881; d) H. W. Gu, R. K. Zheng, X. X. Zhang, B. Xu, *J. Am. Chem. Soc.* **2004**, *126*, 5664–5665.

[8] a) D. Shi, H. S. Cho, Y. Chen, H. Xu, H. Gu, J. Lian, W. Wang, G. Liu, C. Huth, L. Wang, R. C. Ewing, S. Budko, G. M. Pauletti, Z. Dong, *Adv. Mater.* **2009**, *21*, 2170–2173; b) J. H. Choi, F. T. Nguyen, P. W. Barone, D. A. Heller, A. E. Moll, D. Patel, S. A. Boppart, M. S. Strano, *Nano Lett.* **2007**, *7*, 861–867; c) W. J. Rieter, K. M. L. Taylor, H. Y. An, W. L. Lin, W. B. Lin, *J. Am. Chem. Soc.* **2006**, *128*, 9024–9025; d) W. J. M. Mulder, R. Koole, R. J. Brandwijk, G. Storm, P. T. K. Chin, G. J. Strijkers, C. D. Donega, K. Nicolay, A. W. Griffioen, *Nano Lett.* **2006**, *6*, 1–6.

[9] K. L. Holmes, L. M. Lantz in *Methods in Cell Biology, Vol. 63*, Academic Press, San Diego **2001**, pp. 185–204.

[10] a) I. L. Medintz, H. T. Uyeda, E. R. Goldman, H. Mattoussi, *Nat. Mater.* **2005**, *4*, 435–446; b) X. H. Gao, L. L. Yang, J. A. Petros, F. F. Marshal, J. W. Simons, S. M. Nie, *Curr. Opin. Biotechnol.* **2005**, *16*, 63–72; c) X. G. Peng, L. Manna, W. D. Yang, J. Wickham, E. Scher, A. Kadavanich, A. P. Alivisatos, *Nature* **2000**, *404*, 59–61.

[11] a) F. Wang, X. G. Liu, *Chem. Soc. Rev.* **2009**, *38*, 976–989; b) H. S. Qian, H. C. Guo, P. C.-L. Ho, R. Mahendran, Y. Zhang, *Small* **2009**, *5*, 2285–2290; c) M. Nyk, R. Kumar, T. Y. Ohulchanskyy, E. J. Bergey, P. N. Prasad, *Nano Lett.* **2008**, *8*, 3834–3838; d) H. Hu, M. X. Yu, F. Y. Li, Z. G. Chen, X. Gao, L. Q. Xiong, C. H. Huang, *Chem. Mater.* **2008**, *20*, 7003–7009; e) D. K. Chatteriee, A. J. Rufalhah, Y. Zhang, *Biomaterials* **2008**, *29*, 937–943.

[12] a) Y. I. Park, J. H. Kim, K. T. Lee, K.-S. Jeon, H. B. Na, J. H. Yu, H. M. Kim, N. Lee, S. H. Choi, S.-I. Baik, H. Kim, S. P. Park, B.-J. Park, Y. W. Kim, S. H. Lee, S.-Y. Yoon, I. C. Song, W. K. Moon, Y. D. Suh, T. Hyeon, *Adv. Mater.* **2009**, *21*, 4467–4471; b) R. Kumar, M. Nyk, T. Y. Ohulchanskyy, C. A. Flask, P. N. Prasad, *Adv. Funct. Mater.* **2009**, *19*, 853–859.

[13] Y. F. Zhu, W. R. Zhao, H. R. Chen, J. L. Shi, *J. Phys. Chem. C* **2007**, *111*, 5281–5285.

[14] a) A. Abou-Hassan, R. Bazzi, V. Cabuil, *Angew. Chem.* **2009**, *121*, 7316–7319; *Angew. Chem. Int. Ed.* **2009**, *48*, 7180–7183; b) R. Koole, M. M. van Schooneveld, J. Hilhorst, C. D. Donega, D. C. t Hart, A. van Blaaderen, D. Vanmaekelbergh, A. Meijerink, *Chem. Mater.* **2008**, *20*, 2503–2512; c) D. K. Yi, S. S. Lee, G. C. Papaefthymiou, J. Y. Ying, *Chem. Mater.* **2006**, *18*, 614–619; d) S. T. Selvan, T. T. Tan, J. Y. Ying, *Adv. Mater.* **2005**, *17*, 1620–1625; e) Y. Lu, Y. D. Yin, B. T. Mayers, Y. N. Xia, *Nano Lett.* **2002**, *2*, 183–186; f) W. Stober, A. Fink, E. Bohn, *J. Colloid Interface Sci.* **1968**, *26*, 62–69.

[15] C. Barbé, J. Bartlett, L. G. Kong, K. Finnie, H. Q. Lin, M. Larkin, S. Calleja, A. Bush, G. Calleja, *Adv. Mater.* **2004**, *16*, 1959–1966.

[16] a) W. Zhao, J. Gu, L. Zhang, H. Chen, J. Shi, *J. Am. Chem. Soc.* **2005**, *127*, 8916–8917; b) W. Zhao, H. Chen, Y. Li, L. Li, M. Lang, J. Shi, *Adv. Funct. Mater.* **2008**, *18*, 2780–2788; c) D. Niu, Y. Li, X. Qiao, L. Li, W. Zhao, H. Chen, Q. Zhao, Z. Ma, J. Shi, *Chem. Commun.* **2008**, 4463–4465; d) L. Guo, X. Cui, Y. Li, Q. He, L. Zhang, W. Bu, J. Shi, *Chem. Asian J.* **2009**, *4*, 1480–1485; e) F. Chen, W. Bu, Y. Chen, Y. Chi, Q. He, M. Zhu, X. Liu, L. Zhou, S. Zhang, W. Peng, J. Shi, *Chem. Asian J.* **2009**, *4*, 1809–1816.

[17] a) J. C. Boyer, L. A. Cuccia, J. A. Capobianco, *Nano Lett.* **2007**, *7*, 847–852; b) H. Hu, L. Q. Xiong, J. Zhou, F. Y. Li, T. Y. Cao, C. H. Huang, *Chem. Eur. J.* **2009**, *15*, 3577–3584.

[18] a) J. M. Perez, L. Josephson, T. O'Loughlin, D. Hogemann, R. Weissleder, *Nat. Biotechnol.* **2002**, *20*, 816–820; b) J. F. Berret, N. Schonbeck, F. Gazeau, D. El Kharrat, O. Sandre, A. Vacher, M. Airiau, *J. Am. Chem. Soc.* **2006**, *128*, 1755–1761.

[19] L. Q. Xiong, Z. G. Chen, M. X. Yu, F. Y. Li, C. Liu, C. H. Huang, *Biomaterials* **2009**, *30*, 5592–5600.

Received: March 1, 2010
Published online: August 16, 2010

